Journal of Structural Geology xxx (2013) 1–14

Contents lists available at ScienceDirect

Journal of Structural Geology

journal homepage: www.elsevier.com/locate/jsg

Developing sub 5-m LiDAR DEMs for forested sections of the Alpine and Hope faults, South Island, New Zealand: Implications for structural interpretations

R.M. Langridge [a,*], W.F. Ries [a], T. Farrier [b], N.C. Barth [c], N. Khajavi [d], G.P. De Pascale [d]

[a] Dept. of Active Landscapes, GNS Science, P.O. Box 30-368, Lower Hutt 5010, New Zealand
[b] New Zealand Aerial Mapping, P.O. Box 6, Hastings 4156, New Zealand
[c] Dept. of Geology, University of Otago, P.O. Box 56, Dunedin 9054, New Zealand
[d] Dept. of Geological Sciences, University of Canterbury, P.O. Box 4800, Christchurch 8140, New Zealand

ARTICLE INFO

Article history:
Received 11 June 2013
Received in revised form
5 October 2013
Accepted 19 November 2013
Available online xxx

Keywords:
LiDAR
Alpine Fault
Hope Fault
Digital elevation model
Fault segmentation
Structure

ABSTRACT

Kilometre-wide airborne light detection and ranging (LiDAR) surveys were collected along portions of the Alpine and Hope faults in New Zealand to assess the potential for generating sub 5-m bare earth digital elevation models (DEMs) from ground return data in areas of dense rainforest (bush) cover as an aid to mapping these faults. The 34-km long Franz-Whataroa LiDAR survey was flown along the densely-vegetated central-most portion of the transpressive Alpine Fault. Six closely spaced flight lines (200 m apart) yielded survey coverage with double overlap of swath collection, which was considered necessary due to the low density of ground returns (0.16 m^{-2} or a point every 6 m^2) under mature West Coast podocarp-broadleaf rainforest. This average point spacing ($\sim$2.5 m) allowed for the generation of a robust, high quality 3-m bare earth DEM. The DEM confirmed the zigzagged form of the surface trace of the Alpine Fault in this area, originally recognised by Norris and Cooper (1995, 1997) and highlights that the surface strike variations are more variant than previously mapped. The 29-km long Hurunui-Hope LiDAR survey was flown east of the Main Divide of the Southern Alps along the dextral-slip Hope Fault, where the terrain is characterised by lower rainfall and more open beech forest. Flight line spacings of $\sim$275 m were used to generate a DEM from the ground return data. The average ground return values under beech forest were 0.27 m^{-2} and yielded an estimated cell size suitable for a 2-m DEM. In both cases the LiDAR revealed unprecedented views of the surface geomorphology of these active faults. Lessons learned from our survey methodologies can be employed to plan cost-effective, high-gain airborne surveys to yield bare earth DEMs underneath vegetated terrain and multi-storeyed canopies from densely forested environments across New Zealand and worldwide.

1. Introduction

Large magnitude earthquakes that rupture the Earth's surface pose a great risk to human life, buildings and infrastructure, especially along plate boundaries. Where faults rupture the Earth's surface, characteristic tectonic features such as fault scarps can provide insight into location, magnitude, frequency and nature of past earthquakes and fault slip rates (e.g., Sieh, 1978; Wallace, 1968). Therefore, identifying and understanding these tectonic features is important for the accurate location of active faults and the quantification of their activity and contribution to earthquake hazards.

Generally, the most common and cost effective method used to map the location of past surface rupture events has been through the interpretation of stereoscopic aerial photography. However, this method is of limited use in areas covered with dense forest, leading to a disparity in the abundance and accuracy of mapped fault traces. For this reason, it is likely that many fault scarps in remote, tree-covered landscapes remain unidentified (Cunningham et al., 2006; Prentice et al., 2009). In such forested areas, the presence of major faults (i.e. faults that rupture frequently and with a large magnitude) can usually be recognised at least approximately by large cumulative displacements of landscape features at moderate scales, e.g. 1:50,000. However, detailed structural and surficial characteristics of the fault zones, such as the distribution of scarps,

* Corresponding author.
E-mail addresses: r.langridge@gns.cri.nz (R.M. Langridge), w.ries@gns.cri.nz (W.F. Ries), tim@nzam.com (T. Farrier), nic@geology.co.nz (N.C. Barth), narges.khajavi@pg.canterbury.ac.nz (N. Khajavi), snowyknight@gmail.com (G.P. De Pascale).

0191-8141/$ – see front matter © 2013 Elsevier Ltd. All rights reserved.
http://dx.doi.org/10.1016/j.jsg.2013.11.007

secondary faults, fissures, and the precise locations of such tectonic features are often missing.

One of the most significant advances in mapping active faults during the last decade has come from the analysis and interpretation of Light Detection and Ranging (LiDAR) data (Meigs, 2013). LiDAR is a geophysical swath mapping technique that uses light energy from a laser, in this case directed from a plane toward the ground. The frequency of energy returns can be used to resolve point source reflections filtered from varying levels in the landscape, such as tree canopies, under-storey, scrub, human-built structures and the ground surface. Ground returns are typically used to develop digital elevation models (DEMs) that display the surface morphology of the underlying landscape. Thus, LiDAR has the potential to produce 'bare earth' images of landscapes that are otherwise obscured by vegetation (Haugerud et al., 2003; Koehler et al., 2005; Barth et al., 2012).

The transpressive Pacific-Australian plate boundary through New Zealand is dominated by long strike-slip and oblique-slip faults (Fig. 1; Yeats and Berryman, 1987; Berryman and Beanland, 1988; Langridge et al., 2013). In the South Island the main onshore expression of this boundary is the Alpine Fault. To the northeast of the Alpine Fault, upper plate motion is distributed across a plexus of sub-parallel strike-slip faults, including the Hope Fault (Figs. 1 and 2). The Alpine and Hope faults, and even the Wellington Fault, all have a significant proportion of their surface trace length obscured by forest vegetation (>90, 35 and 35%, respectively), which has hindered the accurate mapping of the location and surface expression of these seismogenic faults.

In this study, we use airborne LiDAR to produce high-resolution (e.g., sub 5-m) bare earth DEMs along these faults. In both surveys we specifically targeted remote areas of high research impact that were covered in dense, old growth (primary) forest to test the

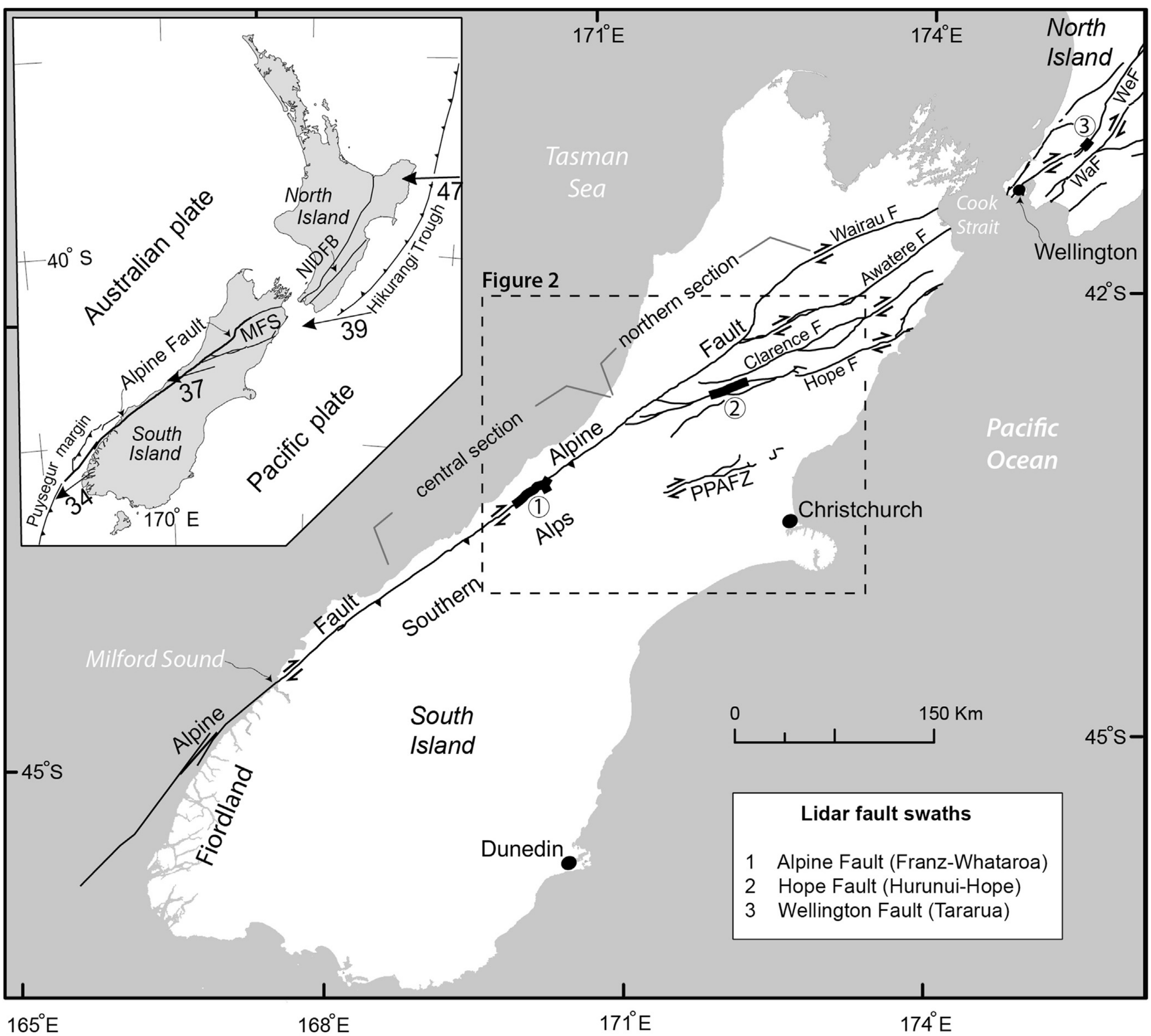

Fig. 1. Active fault map of southern New Zealand highlighting the Alpine Fault, Marlborough Fault System (MFS) and southern part of the North Island Dextral Fault Belt (NIDFB; see also Inset). LiDAR survey areas along the Alpine (1) and Hope (2) faults are marked in bold. Another survey acquired along the Wellington (WeF; 3) Fault is included from Langridge (2011). Other faults are: Wairarapa Fault (WaF); Porters Pass-Amberley Fault Zone (PPAFZ). Inset shows plate tectonic setting of New Zealand. Relative motion between the Pacific and Australian plates is shown in mm/yr from De Mets et al. (1994).

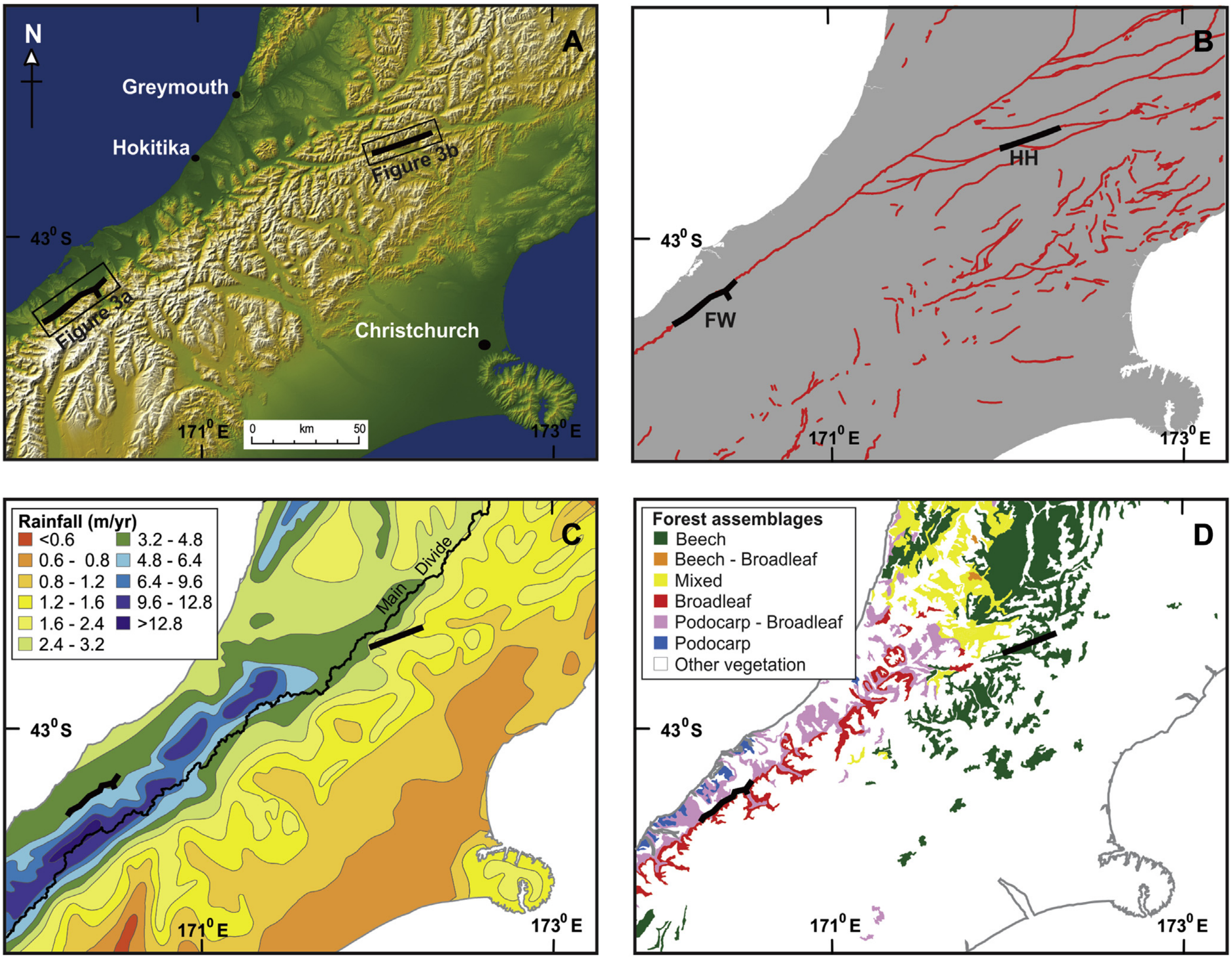

Fig. 2. Physiographic maps of the central South Island covering the LiDAR collection areas along the Alpine (Franz-Whataroa; FW) and Hope (Hurunui-Hope; HH) faults. A. Colour hillshade map across the Southern Alps orogen; B. Active fault map (Source: http://data.gns.cri.nz/af/); C. Contoured rainfall map (Source: www.niwa.co.nz); D. Native forest cover. All other vegetation and land use types are uncoloured (Source: Newsome, 1987).

viability and data quality obtained from airborne LiDAR in the forested and mountainous New Zealand environment for geologic and neotectonic applications. Because this study represents the first time that major elements of the plate boundary have been targeted for LiDAR data collection, we also present examples of the quality of the data and a brief summary of the results that have come from preliminary interpretations of the LiDAR DEMs (see also Barth et al., 2012). These examples show the importance of linking fault mapping to fault segmentation and the earthquake rupture process (e.g. Harris et al., 1991; Wesnousky, 2006). We also quantified the effects of overlapping flight paths on the density of ground point return for various vegetation types, which combined with ground truthing, can provide valuable insights into how future LiDAR campaigns can be planned to maximise the scientific value extracted from them.

1.1. Background

Airborne LiDAR provides a relatively cheap means of obtaining high precision topographic data for use in geomorphic studies of landscape. Digital elevation models derived from airborne LiDAR have been used worldwide in areas of active Quaternary tectonics to verify the location and geomorphic structure of faults (Hudnut et al., 2002; Bevis et al., 2005; Prentice et al., 2009; Barth et al., 2012; Meigs, 2013). LiDAR has been invaluable in detecting fine-scaled geomorphology in environments ranging from dry and unvegetated, e.g. southern and eastern California (Frankel et al., 2007; Arrowsmith and Zielke, 2009; Zielke et al., 2010) to humid and heavily forested climes, e.g. northern California, Pacific Northwest, Taiwan (Haugerud et al., 2003; Chan et al., 2007; Zachariasen and Prentice, 2008). LiDAR-derived DEMs have higher positional and vertical accuracies than DEMs derived from other topographic survey techniques and provide better resolution of geomorphic features, especially under vegetation where other surveying techniques are limited (e.g. RTK-GPS surveying, radar interferometry). However, there remain issues concerning the collection and interpolation of LiDAR data, with respect to ground return density in relation to topography, aspect, and different vegetation cover.

Such remotely collected data can be used to map faults, define offset features, determine slip rates and recognise promising sites for paleoseismic studies (Koehler et al., 2005; Zielke et al., 2010). In addition, repeat LiDAR swaths have been flown following recent surface-rupturing earthquakes along faults to investigate differential movement related to co-seismic ground displacement, e.g., the El Mayor-Cucapah Fault, northern Mexico and the Greendale Fault, New Zealand (Oskin et al., 2012; Quigley et al., 2012; Duffy et al., 2013).

To date, there have been few LiDAR studies in New Zealand that have specifically targeted active faults and much of the LiDAR collected thus far has been flown according to industry standards for local government purposes, i.e. broad swaths at higher elevations and low data densities (Langridge et al., 2006; Begg and Mouslopoulou, 2009; Adams et al., 2011). In addition, many of these studies have not been undertaken across densely forested terrain. Therefore, our study provides an opportunity to test LiDAR collection and processing techniques across a landmass of varying elevation, relief, aspect, rainfall, and particularly diverse vegetation cover specifically targeted towards capturing neotectonic data relating to active faults (Fig. 2). This study focuses on the strategies for airborne LiDAR collection, processing and the resultant ground point densities that were obtained from two surveys located on opposing sides of the Main Divide of the South Island, i.e., west of the divide along the Alpine Fault, and east of the divide along the Hope Fault. In the South Island, the Southern Alps form a major mountain barrier which creates a strong orographic effect from the west (wetter) to the east that results in different vegetation coverage (Fig. 2a, c). The results of a third survey area along the Wellington Fault (Fig. 1; Langridge, 2011) will be briefly discussed as a comparison to the Alpine and Hope fault surveys.

2. Methods

2.1. Survey areas

2.1.1. Alpine Fault (Franz-Whataroa survey)

The dextral-reverse-slip Alpine Fault is one of the major continental transpressive faults worldwide (Berryman et al., 1992; Hodgson et al., 2003; Cox and Sutherland, 2007; Sutherland et al., 2007). ENE-directed tectonic convergence across the central South Island occurs at ~37 ± 2 mm/yr (DeMets et al., 1994; Wallace et al., 2007). In this area, a large proportion (60–80%) of Pacific-Australia plate motion is taken up by the NE-striking Alpine Fault (Norris and Cooper, 2001; Sutherland et al., 2006, 2007), while the remainder is accommodated by the uplift of the Southern Alps and deformation on faults across the width of the South Island margin (Wallace et al., 2007; Beavan et al., 2010; Cox et al., 2012) (Figs. 1 and 2). Along the central section of the Alpine Fault which we chose to survey (Fig. 3a and Fig. 4) both the strike-slip (~25–29 mm/yr) and dip-slip rates of motion are high (~10 mm/yr) (Norris and Cooper, 2001, 2007).

The predominant westerly winds cause heavy rainfall along the western side of the South Island where moist, rising air impinges against the steep western flank of the Southern Alps. Rain is shed onto short catchment systems which leads to intense erosion via landsliding, over a landscape covered by a dense cover of temperate rainforest vegetation (Korup, 2006; Dawson and Lucas, 2011). A positive feedback exists between uplift of the Southern Alps on the hangingwall block of the Alpine Fault, and rapid erosion rates near the fault, which tends to focus continued deformation on the Alpine Fault (Norris and Cooper, 1997; Koons, 1990).

The West Coast coastal plain comprises a remnant glaciomorphic landscape in which short, high-energy rivers traverse the fault-bounded rangefront of the Southern Alps (Fig. 2a and Fig. 3a). Mean annual rainfall for the surveyed area is ~3.8–4.8 m, however, catchment headwaters within the Southern Alps experience from 5 to more than 13 m/yr of rainfall (see http://www.niwa.co.nz; Fig. 2c). The survey area is characterised by high relief with elevation varying from 70 to 890 m a.s.l. (Table 1; Fig. 4). The faceted rangefront is cut by large rivers and steep gullies. Native forests, locally called 'bush', growing along the survey are categorised as mixed podocarp-broadleaf forests that include includes native rimu

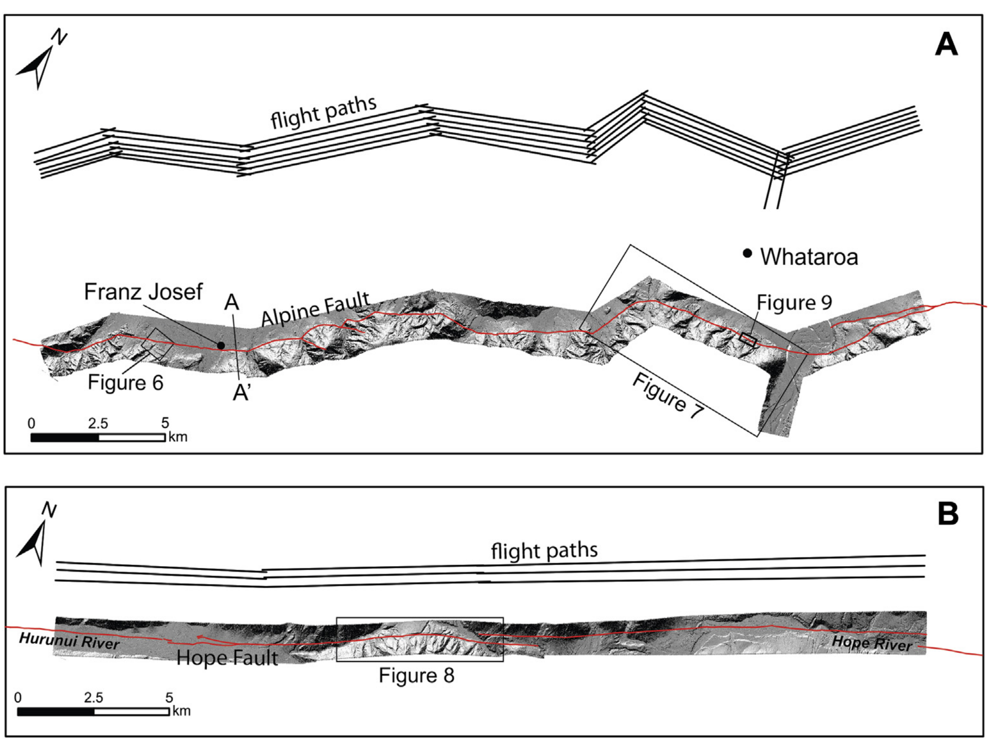

Fig. 3. LiDAR flight paths and resultant hillshade models. A. The Franz-Whataroa survey was composed of seven main segmented flight lines that led to 42 individual flight paths. The resultant 3-m hillshade follows the rangefront of the Southern Alps along the Alpine Fault (red line). Fault location shown comes from Cox and Barrell (2007). Franz Josef township and topographic profile A–A′ used in Fig. 5 are shown. B. Flight lines for the Hurunui-Hope survey and the resultant 2-m hillshade that was produced for the Hope Fault (red line). Fault location shown comes from Langridge and Berryman (2005). Boxes show detailed example areas shown in Figs. 6–8.

Please cite this article in press as: Langridge, R.M., et al., Developing sub 5-m LiDAR DEMs for forested sections of the Alpine and Hope faults, South Island, New Zealand: Implications for structural interpretations, Journal of Structural Geology (2013), http://dx.doi.org/10.1016/j.jsg.2013.11.007

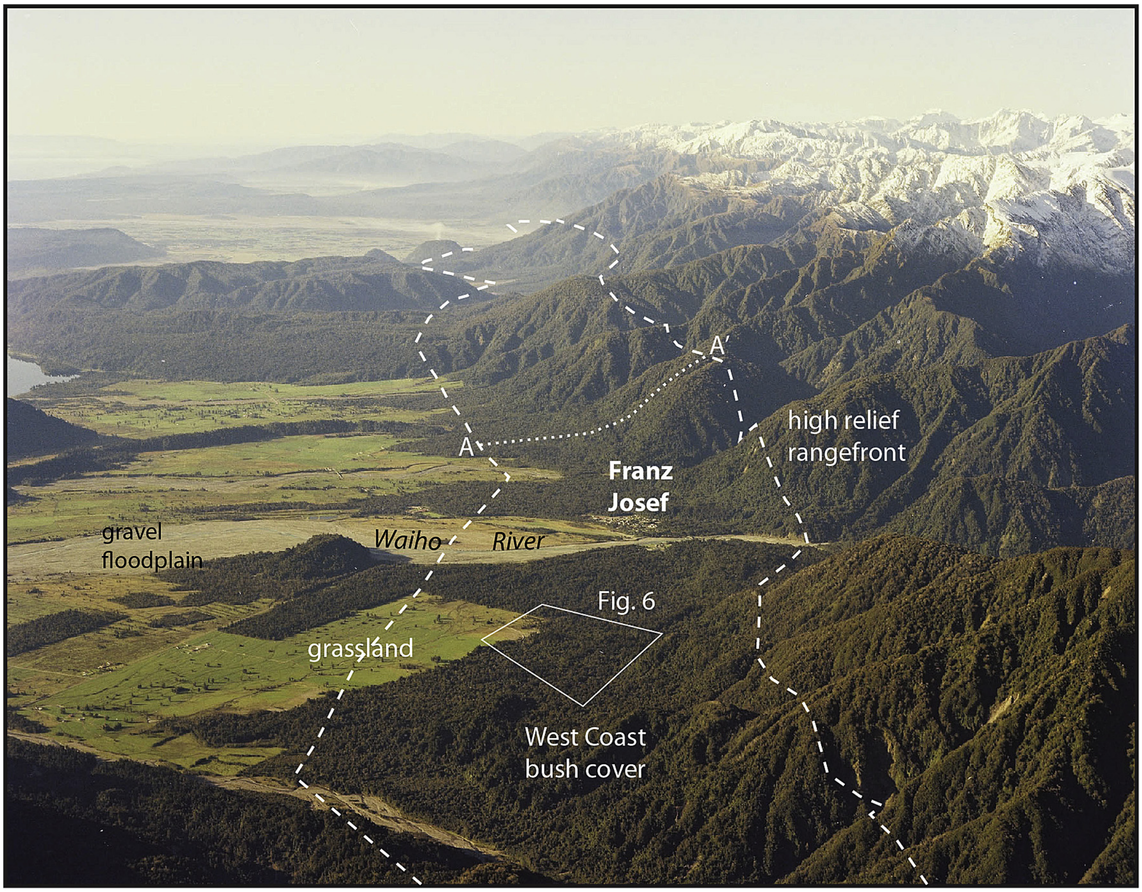

Fig. 4. Oblique aerial photo viewed to the northeast along the Alpine Fault and Southern Alps (peaks at top right). The processed LiDAR swath along the fault is within the white dashed lines, along with the town of Franz Josef at centre. Also shown are different substrate types, such as grassland and bush. (Photo: Lloyd Homer, GNS Science). Profile A–A′ and box show areas of detail covered by Figs. 5 and 6.

(*Dacrydium cupressinum*), matai (*Prumnopytis taxifolia*), kamahi (*Weinmannia racemosa)*, and ponga (tree fern; *Cyathea dealbata*) forming a canopy over a dense understorey dominated by *Pseudopanax* species and supplejack (*Rhipogonum scandens*) vines (Newsome, 1987; Dawson and Lucas, 2011). This especially dense, multi-tiered forest structure provides a test of the effectiveness of LiDAR surveying. Lowland areas below the rangefront have typically been cleared for grassland dairy farming and now lack extensive tree cover. Scrub, dominated by 'Tutu' (genus Coriaraia), Hebe, Coprosma and Dracophyllum, covers areas where young alluvial terraces have been colonised or where forest is regenerating. The only significant area within the LiDAR swath covered by buildings is the town of Franz Josef (Fig. 5).

Table 1
Natural parameters and data related to the lidar surveys.

	Alpine Fault (Franz-Whataroa)	Hope Fault (Hurunui-Hope)
Latitude[a]	43° 20′ S	42° 39′ S
Elevation range (m[b])	70–890	520–1240
Typical relief (m)	400–600	200–400
Rainfall (mm/yr)	3800–4800	1500–3000
Dominant vegetation cover	Mixed podocarp-broadleaf forest	Beech forest
Percent ground returns	9.8	16.9

[a] Latitude of central point within swath.
[b] Metres above sea-level.

In this study, we have flown, processed and analysed LiDAR data along a 34 km long stretch of the central Alpine Fault extending roughly between Franz Josef and Whataroa townships (Fig. 3a). This stretch of the fault was targeted to test the viability of LiDAR as a tool to obtain a 'bare earth' DEM through West Coast native forest,

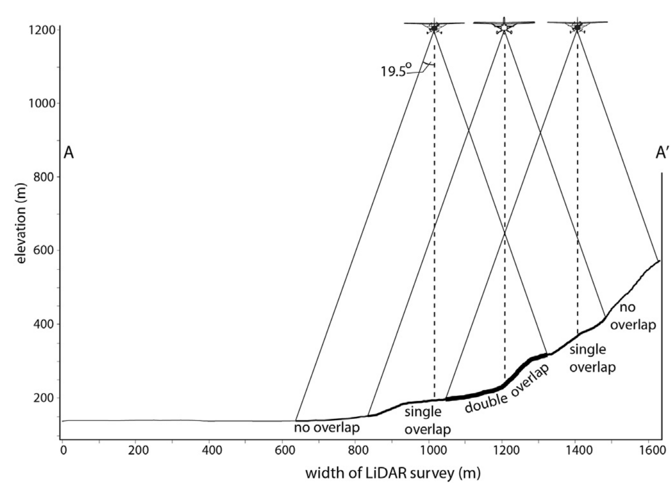

Fig. 5. Schematic diagram showing the elevation and flight path profile along A–A′ from the Alpine Fault LiDAR survey. These three of six flight lines show the broad effects of topography on the survey band width. Flight lines were 200 m apart which produces bands of no overlap and single or double overlap of point collection.

which is recognised as some of the densest forest in New Zealand and which has been a significant obstacle to detailed geological mapping and neotectonic study of the Alpine Fault (e.g., Cox and Barrell, 2007) (Fig. 2d). Some applications of this LiDAR dataset have already been introduced (Langridge, 2011; De Pascale and Langridge, 2012a; Barth et al., 2012).

2.1.2. Hope Fault (Hurunui-Hope survey)

Located to the east of the Main Divide, the dextral-slip Hope Fault is part of the Marlborough Fault System, a zone of distributed strike-slip faulting (Fig. 1 and Fig. 2b) (Holt and Haines, 1995; Van Dissen and Yeats, 1991; Langridge et al., 2003; Yeats and Berryman, 1987; Berryman et al., 1992; Wallace et al., 2007). Dextral slip rates in the east along the Conway segment of the Hope Fault are high (18 ± 8 mm/yr; ∼23 ± 4 mm/yr) (McMorran, 1991; Langridge et al., 2003), but are somewhat lower in the west (14 ± 3 mm/yr; ∼10–13 mm/yr; Cowan, 1990; Langridge and Berryman, 2005) where motion is partitioned between the Hope and Kakapo faults.

LiDAR has already been proven to be an effective tool for mapping the eastern part of the Hope Fault (Beauprêtre et al., 2012). At the eastern end of the fault, the orographic rainshadow of the Southern Alps has brought about a landscape that is semi-arid, largely grass-covered and sparsely forested. Here, mean annual rainfall is 1.0–1.6 m (Fig. 2c). In comparison, along the Hurunui segment of the Hope Fault where we established our second survey, average annual rainfall is ∼1.5–3.0 m; intermediate between that for the West Coast and eastern Marlborough (Fig. 2d).

Apart from areas of active alluviation and grasslands, the landscape is covered by relatively open native beech (*Nothofagus*) forest with a thin understorey (Fig. 2d). The forest is characterised by red beech (*Nothofagus fusca*), silver beech (*N. menziesii*) and mountain beech (*N. solandri* var. *cliffortiodes*), which all share a similar tree structure (Fig. 2d) (Wardle, 1984; Langridge et al., 2007). Scrub in the low-lying areas of alluvial valleys within this survey is dominated by Matagouri (*Discaria toumatou)* bushes.

A 29 km long LiDAR survey was flown along the western part of the Hope Fault extending from the Hurunui to the Hope River (Fig. 3b) (Langridge and Berryman, 2005). Local parameters for rainfall, elevation, relief, and vegetation type for this area are displayed in Table 1. A west to east gradient in rainfall exists between the western end of the swath (∼2.4–3.0 m annually) and the eastern end of the swath (∼1.5–1.8 m annually; see http://www.niwa.co.nz).

2.2. Flight planning

To obtain the best possible results from the airborne LiDAR a data collection plan was developed for each fault. The first part of this plan was to define flight paths with the data provider, New Zealand Aerial Mapping Ltd (NZAM). Project budget dictated that the target width around each fault was limited to a corridor of ∼±800 m in width (Fig. 3). In both cases we used regional geological maps and the national active faults database as a basis for defining the centre line of the LiDAR swaths (e.g., Nathan et al., 2002; http://data.gns.cri.nz/af). The natural parameters of each study area are outlined in Table 1 and discussed below.

Different flight path spacings were selected for each survey based on the forest type and density, with a view to improve the number of ground returns in areas where several pre-lidar reconnaissance trips indicated dense, multi-tiered vegetation cover and very high relief (e.g. Langridge and Berryman, 2005; Langridge and Ries, 2010). Flight path spacing was particularly important along the Alpine Fault where the steepness and density of forest cover were highest.

The outcome was a flight plan for the Franz-Whataroa survey that comprised six, parallel, zigzagged lines spaced ∼200 m apart (Fig. 3a). The zigzagged form of the flight plan was designed to follow the segmented trace of the Alpine Fault in this region as previously identified by Norris and Cooper (1995). The middle of the survey strip was centred just to the southeast of the mapped trace of the fault in order to not only capture the primary zone of faulting and offset features, but to focus on the hangingwall side of the fault, where deformation was expected to be greater (Cox and Barrell, 2007; Barth et al., 2012). Two additional short lines were flown in the Whataroa valley for use by the Deep Fault Drilling Project (Sutherland et al., 2012, Fig. 3a).

2.3. Data acquisition

LiDAR data were acquired with an Optech ALTM3100EA instrument flown from a light plane at a typical altitude of ∼1200 m above ground level (a.g.l.; Fig. 5), i.e., which had to be adjusted for the higher elevation parts of both surveys. To aid the processing of the data, colour orthophotographs were taken in conjunction with the LiDAR using an integrated Rollei AIC camera. The Optech scanner field of view was set to 39°, which produced a swath width of ∼390 m either side of the instrument above flat ground.

For the Franz-Whataroa survey, individual flight swaths spanned this width over flat terrain meaning that there was almost complete single-overlap between sets of adjacent swaths; the exception being the two outermost strips along the swath (Fig. 5). In the middle part of the swath double overlap of data was achieved. In addition, small areas of triple overlap of data, i.e. four discrete scans of the same area, were also obtained around the six bends in the swath (Fig. 3a). Overlap of flight swaths is normal practice; however, in this case it was deemed important to the success of the Franz-Whataroa LiDAR survey to obtain some double overlap of flight lines due to the density of the West Coast bush.

For the Hurunui-Hope survey, the flight collection plan comprised three flight lines at an average spacing of ∼275 m (Fig. 3b). This is a default flight line spacing for LiDAR collection used for the forest industry and which was deemed suitable for beech forest cover (Adams et al., 2011). This simple flight plan was aided by the fact that the Hope Fault here was known to be relatively straight compared to the central-most part of the Alpine Fault where the Franz-Whataroa survey was staged.

Independent ground surveys established a reference control network that tied the data into the national geodetic reference system of New Zealand (NZGD2000). Data points have an x–y positional accuracy of ±0.30 m and a vertical accuracy of ±0.15 m. The data supplied by NZAM comprised point clouds of ground and unclassified (above ground) returns, used to develop a bare-earth DEM and hillshade model. Also supplied were 0.5 m contours developed from Triangular Irregular Networks (TIN) generated from the ground return point cloud.

2.4. DEM construction and interpolation

For unforested areas, such as over grassland and gravel substrates, the number of cleaned ground returns was approximately equal to the signal input, i.e. ∼100% returns. In contrast, over forested land up to 3–4 times the number of total returns were typically counted. In these cases, unclassified returns were being collected from different levels of the forest, e.g. from the canopy, sub-canopy, under-storey, and also the ground. All unclassified returns were then filtered in-house by NZAM.

A DEM is a GIS-based, raster grid of elevation values usually obtained by interpolation between adjacent sample points. Resolution of a DEM refers to the grid size of the DEM; smaller grids

Please cite this article in press as: Langridge, R.M., et al., Developing sub 5-m LiDAR DEMs for forested sections of the Alpine and Hope faults, South Island, New Zealand: Implications for structural interpretations, Journal of Structural Geology (2013), http://dx.doi.org/10.1016/j.jsg.2013.11.007

represent higher resolution and more detail. Determination of the cell size of a DEM is a fundamental component for DEM generation and spatial analysis. The main goal is to produce the best representation of a terrain surface without introducing artefacts from interpolation, i.e., the source data density constrains the resolution of the DEM. A common method for determining the cell size of a DEM has been defined by Hu (2003). The grid size of a DEM can be estimated by:

$$s = \sqrt{\frac{A}{n}} \tag{1}$$

where s is the estimated cell size (typically in m), n is the number of sample points and A is the area containing the sample points. The formula above was used to calculate the estimated cell size for both the Alpine and Hope datasets (Table 2).

This aforementioned method for estimating DEM cell size works well for datasets with homogeneous vegetation and therefore homogeneous point densities. However, areas with variable vegetation are likely to produce highly variable ground return densities and therefore using an average for the entire dataset is likely to estimate a cell size smaller than desired in areas under thick vegetation with low point densities.

To analyse the variability of point densities, subsets of the following vegetation types or substrates were extracted from the ground return point cloud. For the Franz-Whataroa survey these were grassland, scrub, gravel (river beds) and podocarp-broadleaf bush. For the Hurunui-Hope survey, subsets were extracted from areas of grassland, scrub, gravel, and beech forest. Subset areas were chosen through identification from the orthophotographs. Twelve 50 m × 50 m (0.25 ha) areas were selected for each substrate type. Table 2 shows the point densities for each subset or substrate and the estimated cell size using equation (1). From this analysis, the cell size for each dataset was determined. This was then used as the input for interpolating a DEM for each area.

Interpolation is a process of predicting the value of a grid of cells. Common interpolation methods include Nearest Neighbour, Inverse Distance Weighting (IDW) and Kriging. There is no single interpolation method that can be used exclusively for all purposes, though one technique will have more advantages under certain data conditions. For example, a DEM produced for hydrological modelling needs to be ‘hydrologically’ correct (i.e. the surface of the DEM needs to ensure water flows downhill and best approximates the actual drainage). One of the end goals of this study is to accurately locate and map active fault traces. It is therefore very important to ensure the interpolation methods used does not smooth over subtle changes in elevation that may have been produced by faulting or erosion. With this in mind, it is also important to ensure linear artefacts produced from the interpolation process are also limited to avoid interpreting interpolated artefacts as geomorphic features. The balance between smoothing and avoiding artefacts is hard to achieve and in many cases relies on a good working knowledge of the interpolation method, the input parameters, as well as trial and error (Arrowsmith and Zielke, 2009).

DEMs produced for the two study areas were interpolated with IDW using a power value (significance of surrounding points in the interpolated value) of 2 and a search radius of 12 points with a maximum radius of 20 m. This method and input parameters provided a good balance between interpolating subtle changes in slope without producing large anomalous artefacts in areas of low point densities. This does not however, imply that the DEMs produced for this study are free from error or artefacts.

3. Lidar survey results and DEM creation

The purpose of this section is to describe how we defined the grid spacing for the two DEMs. In each survey area we selected a representative area in which to undertake an analysis of the point density and point spacing of the datasets. The results of DEM analysis allowed us to distinguish between the LiDAR characteristics and data quality of podocarp-broadleaf versus beech forest cover as these were the dominant substrate types along both survey areas. LiDAR ground return points from each swath were used to create DEMs that were relevant to the point densities and spacings that are shown in Table 2.

3.1. Franz-Whataroa survey

Across the measured 0.25 ha sample boxes, the average ground returns per m^2 were high for gravel and grassland (1.63 m^{-2} and 1.28 m^{-2}, respectively), but significantly lower for scrub (0.53 m^{-2}) and especially for podocarp-broadleaf forest (0.16 m^{-2}). The latter is equivalent to having a ground return point about every 6 m^2. The average ground returns across the entire survey were 0.40 m^{-2} which yields an estimated cell size of 1.59 m using Equation (1). However, considering the high proportion of the study area covered by bush (∼90%), it is more efficient to consider the estimated cell size under podocarp-broadleaf forest (Fig. 6). In this case, equation (1) yields an estimated cell size of 2.52 m (Table 2). In detail, the point cloud underneath the forest was not evenly distributed, with areas of clustered points in more open spaces contrasting other areas with low point densities (Table 2). Considering the extremes in point spacing under forest (rather than the mean), we inferred that the most suitable grid size for a DEM and hillshade model of the area is 3-m. Despite the low ground return ratio, i.e., ∼9.8% returns compared to gravel substrate, we inferred from extensive ground truthing in the forest, that the resulting DEM provides a valid interpretation of the ground topography. Fig. 6 highlights the difference in precision between the national scale 25-m DEM versus the 3-m LiDAR DEM and its accompanying colour orthophotograph.

Table 2
Ground return point data from the LiDAR surveys.

Sample area *substrate*	No. of 0.25 ha sample areas	Area (ha)	Ground return points (m^{-2})	Estimated cell size (m)	Total returns	Unclassified returns (m^{-2})
Franz-Whataroa	Entire survey	6025.8	0.40	1.59	–	–
Gravel	12	3	1.63	0.78	49210	1.64
Grassland	12	3	1.28	0.88	38806	1.29
Scrub	12	3	0.53	1.37	131859	4.40
Podocarp-broadleaf bush	12	3	0.16	2.52	180227	6.01
Hurunui-Hope	Entire survey	3543.9	0.56	1.34	–	–
Gravel	12	3	1.47	0.82	73073	2.44
Grassland	12	3	1.60	0.79	70477	2.35
Scrub	12	3	0.78	1.13	78352	2.61
Beech Forest	12	3	0.27	1.93	108971	3.63

Please cite this article in press as: Langridge, R.M., et al., Developing sub 5-m LiDAR DEMs for forested sections of the Alpine and Hope faults, South Island, New Zealand: Implications for structural interpretations, Journal of Structural Geology (2013), http://dx.doi.org/10.1016/j.jsg.2013.11.007

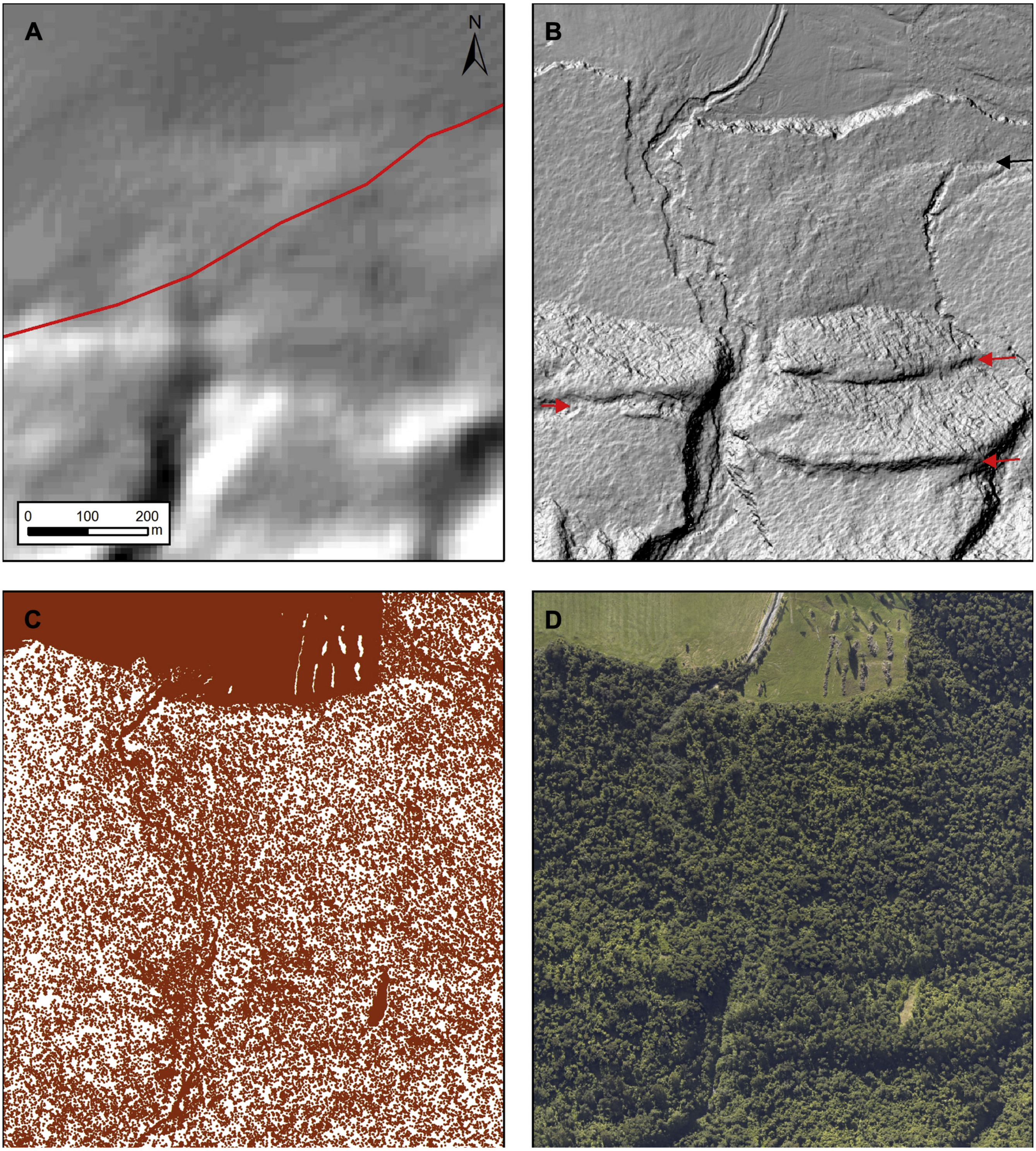

Fig. 6. Visual comparisons of data coverage at Lavender Farm, west of Franz Josef. A. national scale 25-m DEM with trace of the Alpine Fault (red line) as shown on Cox and Barrell (2007). B. 3-m LiDAR hillshade model highlighting geomorphic features including strike-slip (red arrows) and thrust (black arrow) fault traces. C. Ground return point cloud for the same area highlighting differences between grass and bush substrates. D. Orthophotograph showing actual vegetation cover.

An interesting product of our analyses is the recognition that up to 6 m^{-2} unclassified returns were collected from each sample shot (c. ~1.64 m^{-2} for gravel substrates; Table 2). This means that there are about four times the number of returns from dense bush, which highlights the multi-tiered nature of the forest structure.

3.2. Hurunui-Hope survey

Across the measured 0.25 ha sample boxes along the Hurunui-Hope survey, the average ground returns per m^2 were high for gravel and grassland (1.47 m^{-2} and 1.60 m^{-2}, respectively), but significantly lower for scrub (0.78 m^{-2}) and for beech forest (0.27 m^{-2}). The latter is equivalent to having a ground return point about every 4 m^2 on average. The average ground returns per m^2 across the entire survey were 0.56 m^{-2} which yields an estimated cell size of 1.34 m using equation (1). However, considering the high proportion of the study area covered by forest, it is again more useful to consider the estimated cell size under beech forest. In this case, Equation (1) yields an estimated cell size of 1.93 m (Table 2).

Therefore, for this survey a robust 2-m DEM was generated across beech forested terrain (Fig. 3b). A 1-m DEM revealed a similar amount of geomorphic detail as the 2-m DEM, but suffered from some processing artefacts such as facets, blisters and pockmarks. These were particularly evident across the steep, heavily forested rangefront slopes. We observe that the entire width of fault deformation was captured within the 1.3 km width of the Hurunui-Hope swath, validating our choice of using only three flight lines spaced every ~275 m (Fig. 3b).

4. DEM-based characterisation of geomorphic features

4.1. The Alpine Fault – Mt Price and Lavender Farm areas

The Franz-Whataroa DEM offered the opportunity to observe the complex zone of deformation in the hangingwall block of the Alpine Fault, including primary traces of the fault that were previously unrecognised (De Pascale and Langridge, 2012a; Barth et al., 2012).

Fig. 6 highlights the geomorphic detail observed from the 3-m DEM compared to the national scale 25-m DEM. In this area west of Franz Josef, the difference between the point density under bush, versus grassland, hedgerows or landslips is distinct (Fig. 6c). In the 25-m DEM (Fig. 6a), geomorphic features including the Alpine Fault, are poorly characterised. In particular, the previously mapped geologic fault trace cannot be resolved on this DEM. That is, at scales of 1:50,000 or more only a general view of the actual fault location, strike and complexity is realistic and past fault mapping efforts have been limited by the vegetation (Cox and Barrell, 2007; Norris and Cooper, 1995). However, from the 3-m DEM it is clear the fault occupies a wider zone of deformation, with partitioning into ~east-west-striking strike-slip faults that create and translate topography, and a frontal thrust trace that takes up the outboard dip-slip component of fault motion (Barth et al., 2012). Field reconnaissance shows that these strike-slip fault bounded ridges are draped by deformed morainic deposits from the last glacial. The frontal thrust trace is highlighted by a topographic scarp into which a small stream has incised (Fig. 6b).

Fig. 7 highlights the LiDAR coverage centred about Mt Price between Gaunt Creek and the Whataroa River. Along the rangefront of the fault west of the river, alluvial terraces and fans, risers, ridgelines, scarps, lineaments, folds were recognised and these helped to define the location and style of faulting (Fig. 7c; Barth et al., 2012). The character of the Alpine Fault zone in this locality is expressed by 2 or 3 sub-parallel, active ENE-striking fault traces each separated by 100–300 m. These faults have a dominant dextral-slip style of motion, based on the recognition of dextrally deflected streams and spurs (ridgelines) and uphill-facing scarps. This is particularly true of the area between the Matainui and Mint Creek catchments. The scale of these deflections ranges from tens to hundreds of metres across each fault trace implying that these faults carry a significant proportion of the dextral motion across the central Alpine Fault (Langridge, 2011; Norris and Cooper, 2001). The dextral-slip character of this 5 km stretch of the fault was previously known (Read, 1994; Norris and Cooper, 1995, 1997; Cox and Barrell, 2007); though, was much more coarsely and incompletely resolved before the availability of this dataset. We found no small (sub-decametre) sized displacements along this short 5 km reach of the fault where there were multiple strike-slip fault traces. However, geomorphic features with potential single-event displacements were identified in other areas along the Franz-Whataroa survey where the fault zone is less complex (De Pascale and Langridge, 2012b).

The surface projection of the Alpine Fault zone is obscured across low-lying terraces of the Whataroa River and active drainages adjacent along the rangefront such as Matainui Creek (Fig. 7c). This is because the presently abandoned alluvial terrace of the river and the fans that grade to it were rejuvenated following the last surface-rupturing earthquake along the Alpine Fault in ~1717 A.D. (Wells et al., 1999, 2001; Yetton, 2000; Berryman et al., 2001).

A prominent bend in the surface trace of the Alpine Fault is also highlighted in Fig. 7. In the area north of Gaunt Creek, NNW-striking fault traces are mapped bounding the rangefront to the west of Mt Price. One of these traces was exposed near Gaunt Creek

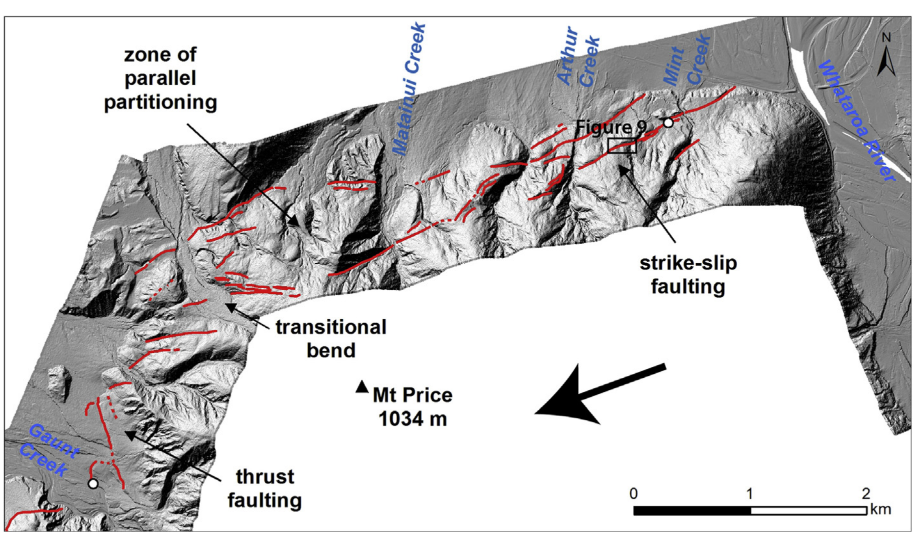

Fig. 7. Hillshade model along the Alpine Fault between the Whataroa River and Gaunt Creek. The LiDAR strip highlights the transition from thrust faulting to a transitional bend characterised by parallel partitioning, into a zone of strike-slip faulting in the east near the river. Note the large dextral offsets of spurs and creeks between Matainui and Mint creeks. White circles identify paleoseismic sites. Large black arrow marks the motion direction for the Alpine Fault.

Please cite this article in press as: Langridge, R.M., et al., Developing sub 5-m LiDAR DEMs for forested sections of the Alpine and Hope faults, South Island, New Zealand: Implications for structural interpretations, Journal of Structural Geology (2013), http://dx.doi.org/10.1016/j.jsg.2013.11.007

and a paleoseismic study was undertaken to document the faulting at that locality (De Pascale and Langridge, 2012a). The main fault associated with this exposure was a low angle thrust with an attitude of 334/26° SE. Thirteen other attitudes measured from within faulted and fractured mylonites in the hangingwall of this exposure are also consistent with NNW-striking and WSW-directed thrusting, i.e. sigma-1 oriented at c. 072/10°.

4.2. The Hope Fault west of Three Mile Stream

Fig. 8 shows a ~5 km long section of the Hurunui-Hope LiDAR survey between Three Mile and McMillan streams. This area is in the higher elevation, central part of the survey where beech forest covers most of the landscape (Fig. 8b). The 2-m DEM has enabled the recognition and mapping of alluvial terraces and risers, spurs, and alluvial fans, and helped define the main fault traces related to the Hope Fault (Khajavi et al., 2012). Broad fans and terraces that emanate from the Macs Knob range were deposited after the Last Glacial Maximum (LGM). Later, incision during the Holocene by tributaries of Three Mile and McMillan streams cut the fans forming a complex of gullies and small valleys (Barrell et al., 2011; Langridge and Berryman, 2005).

In this area, the Hope Fault is expressed by a single, main ENE-striking fault trace (Fig. 8). Deflected streams and offset terrace risers, fans and spurs confirm that the Hope Fault is a dextral-slip fault and that post-LGM landforms have been offset horizontally by tens to more than 100 m. Langridge and Berryman (2005) used the scale of displaced landforms in this area from aerial photographs to estimate a Holocene dextral slip rate of ~10–13 mm/yr. A distinct advantage for future displacement and slip rate studies is the clarity with which the fault and offset features are expressed in the DEM (Fig. 8), giving greater confidence in the size of displacements, the measurement uncertainty, and the relative age of landforms. Curvature of the main fault trace (slightly concave to the south) suggests that the Hope Fault dips steeply to the south in this area. In addition to the main fault trace, subsidiary and secondary faults, and fault stepovers can be mapped to the east of the Three Mile Stream area. In many places such structures can be mapped out to a distance of ~300 m from the main trace, which defines the probable width of deformation throughout the Holocene (Langridge, 2011; Khajavi et al., 2012).

5. Discussion

5.1. Aspects of data collection issues

The data collection and processing strategy devised for this project enabled us to generate reasonable and high quality, sub 5-m bare earth DEMs across the Franz-Whataroa (3-m DEM) and Hurunui-Hope (2-m DEM) survey areas. A higher resolution DEM was possible for the Hurunui-Hope survey even though the line spacing and resultant levels of swath overlap were diminished. The number of unclassified returns (i.e. all returns including ground returns) for the West Coast mixed podocarp-broadleaf bush was ~6 m^{-2} returns (four times that from gravel), indicating the multi-tiered structure of the canopy in this area. In comparison, the number of unclassified returns for beech forest was ~3.63 m^{-2}, indicating a more open forest structure (~2 returns per sample shot). Above all these results highlight the difference in undertaking LiDAR surveys under these forest types of different density either side of the Main Divide.

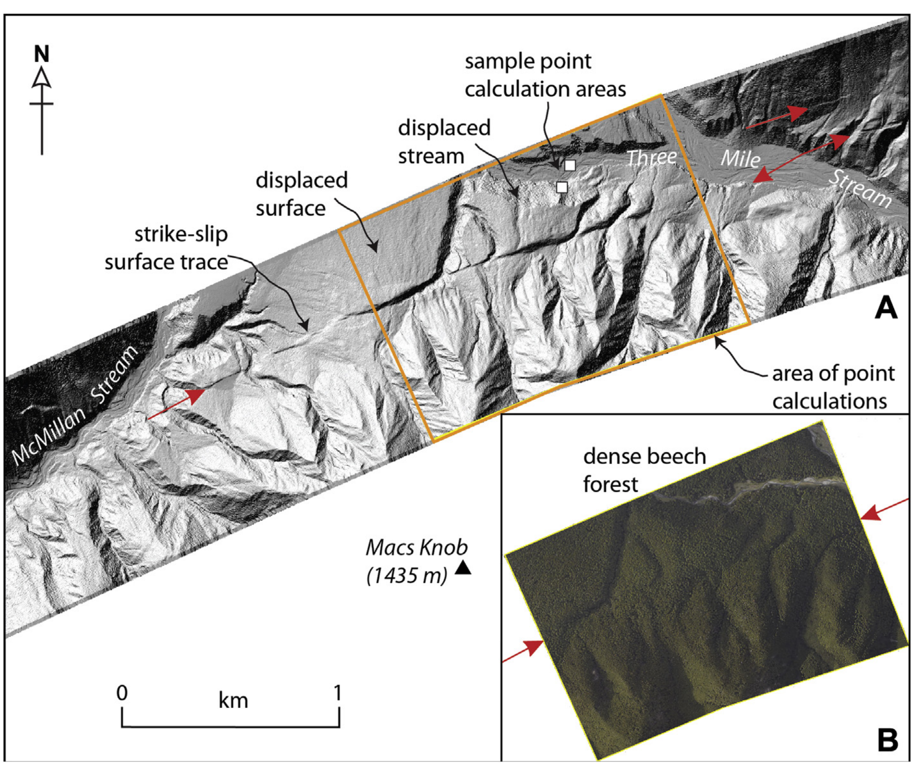

Fig. 8. A. 2-m LiDAR-derived hillshade model of the ENE-striking Hope Fault between the Hurunui and Hope river catchments highlighting the main fault trace (red arrows), displaced landforms and geographic features. A c. 100 m left step in the main fault expression occurs at top right. The white boxes show typical 0.25 ha areas where analyses of LiDAR point data were undertaken. B. Colour orthophotograph covering the same area as the orange box and highlighting beech forest cover.

Topography (aspect, slope and elevation of the ground surface) has also been identified as influencing the number of ground returns. The main effect of steep slopes is to limit the swath width of point collection and increase the likelihood of erroneous ground returns. The narrowing of the 'footprint' of data collection is clearly evident at the edges of the survey where elevations are higher and relief increases. However, the decreased swath width does not overtly affect the quality of the survey data other than to reduce the area that was surveyed.

Qualitative analysis of the ground return point cloud for both surveys show areas where ground returns are limited on some aspects due to parallel flight direction combined with steep slopes producing areas shadowed by the topography, e.g. hillslopes either side of northeast-trending spurs. Generally, the recovered point density (and thus data quality), was less in steep areas (e.g., terrace edges along the rangefront of the Alpine Fault), especially where these areas are incised by gullies. While this influence reduces the number of ground returns on some slopes the overall average point spacing does not vary significantly enough to cause interpolation errors and therefore erroneous topographic artefacts.

Our strategy to overcome the effect of especially dense forest cover in the high rainfall Franz-Whataroa survey area was to increase the number and degree of overlap between the adjacent flight lines. Without doubt, for the Franz-Whataroa swath, the double overlap strategy was essential toward developing at best a 3-m DEM. While this strategy was essential for this central-most part of the Alpine Fault, we note that the default LiDAR collection parameters for forested areas (e.g., 275 m flight line spacing) should be applicable to the northern Alpine Fault, where the natural conditions are more like the western Hope Fault (Fig. 1 and Fig. 2d). This would allow for the generation of robust 2-m DEMs of high quality along the northern section of the Alpine Fault at a lessened cost compared to that for the Franz-Whataroa survey.

Data from both surveys indicate that 1-m DEMs could be generated in open areas of gravel and grassland where ground return values are high (Table 1). This means that for site-specific studies, e.g., where a fault under forest emerges into grass-covered areas, constructing a 1-m DEM from a subset of the data cloud is valid. To test the validity of our selected DEM cell sizes we developed 1-m DEMs for both surveys. We observed that for areas under podocarp-broadleaf bush, processing (interpolation) artefacts such as facets were locally apparent where point densities were relatively low, which validated our cell size choices. Fig. 9 shows the differences in DEM or image quality between 0.5-, 1-, 2- and 3-m DEMs created for a heavily forested area west of the Whataroa River (Fig. 7). Pockmarks and blisters are evident on the 0.5- and 1-m DEMs, which highlights that the DEM is over-interpolated relative to the data. In contrast the 2- and 3-m DEMs can appear pixelated at detailed scales (Fig. 9).

As part of a wider national project, a third short (6 km) LiDAR survey was collected along a forested portion of the Wellington Fault within the Tararua Range (Fig. 1) (Langridge, 2011; Langridge et al., 2005). In this area the relief is similarly high (300–500 m), rainfall is intermediate between the two South Island surveys (~2.5–3.0 m/yr), and the rangefront of the fault is covered by a mixed lowland podocarp-broadleaf-beech forest (Newsome, 1987) with a significant component of ponga (tree fern; *C. dealbata*). This Tararua forest assemblage is intermediate in density compared to the two South Island forested areas. In this case, with five flight lines spaced at distances of ~240 m, the average ground returns under this forest assemblage was ~0.19 m^{-2}. As with the Franz-Whataroa survey, this level of data return could be used to develop a robust 3-m DEM. This allowed for the recognition of a multi-event, transpressive fault scarp in the Waiohine River valley under dense forest for the first time (Langridge, 2011).

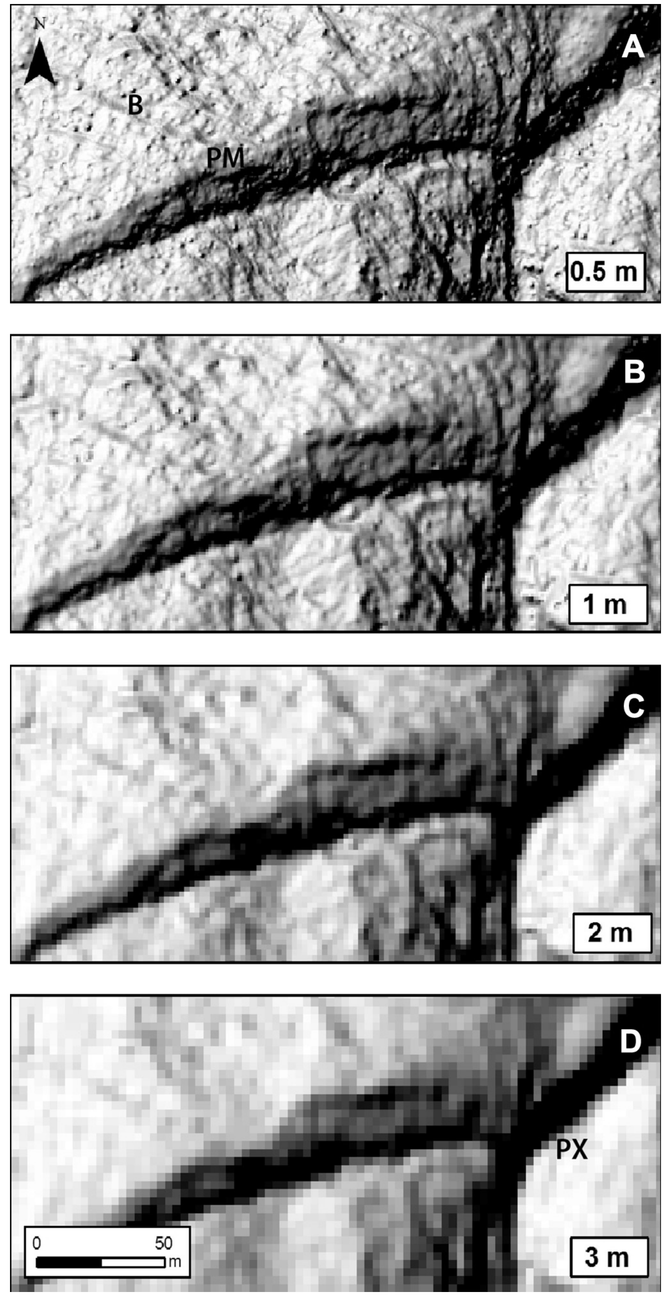

Fig. 9. Examples of DEMs created at different grid sizes for the same area west of the Whataroa River. A. and B. 0.5-m and 1-m DEMs. These are characterised by pockmarks (PM) and blisters (B) in the data. C. and D. 2-m and 3-m DEMs.

5.2. Implications for active fault studies

We observe that the pattern and style of surface faulting expressed along the central-most Alpine Fault is consistent with the fault segmentation model shown by Norris and Cooper (1995, 1997) and on regional geology maps (Cox and Barrell, 2007). A key difference with the latter is the level of detail at which the fault can now be mapped compared to previous scales (see Fig. 3c.f. Fig. 6). Other important differences were observed from the LiDAR DEM, such as the number of strike-slip fault traces within the zone of active fault deformation in the Mint to Arthur creek area (2-3 main traces), where fault strikes of 070 ± 10° were evident (Fig. 7). The average strike of the Alpine Fault along its length is 055°. Thrust fault scarps with strikes of 350 ± 10° were evident in the Gaunt Creek area (De Pascale and Langridge, 2012a). Between these two end-members (north of Gaunt Creek: thrust-dominated; west of Whataroa River: dextral-dominated), the area west of Matainui Creek is highlighted by a transitional bend of up to 600 m width where it appears that parallel partitioning of the Alpine Fault is occurring. Here, the surface form of the Alpine Fault zone is characterised by a set of outboard reverse to thrust faults with strikes that curve to compensate for the surface bend in the fault trace; and ~east-west striking, closely-spaced strike-slip faults within the hangingwall block (Fig. 7). All these structures are potentially consistent with the overall oblique motion direction of the Alpine Fault in this area (c. 070°). In addition, this transitional bend is associated with the highest peak (Mt Price) within 1 km of the Franz-Whataroa survey locally. These results confirm the fault segmentation and parallel partitioning scheme of the central-most part of the Alpine Fault (Norris and Cooper, 1995, 1997; Barth et al., 2012), and highlight the advances that can be made in understanding the structural geology of the fault using a high resolution DEM (Meigs, 2013). Furthermore, the LiDAR hillshade highlights that the map and strike variations shown by the Norris and Cooper (1995, 1997) models can be even more extreme in map view than predicted.

The DEMs produced from this study have great potential for use in neotectonic and hazard studies. Along the Alpine Fault, we have already been able to identify future paleoseismic sites and confirm the recent activity of north-striking thrust traces such as those at Gaunt Creek (Fig. 7; De Pascale and Langridge, 2012a). Paleoseismic studies at Mint Creek will test the viability of uphill-facing scarps as locales where late Holocene sediments accumulate and preserve evidence of recent faulting events. In addition, detailed fault mapping such as this can be useful for considering fault segmentation and the endpoints of fault ruptures (Harris et al., 1991; Wesnousky, 2006).

With respect to displacement and slip rate studies, it is important to understand the strengths and limitations of the LiDAR-derived DEM. For example, the 3-m cell size from the Alpine Fault survey means that this technique will revolutionise the collection and interpretation of multi-event displacements along the fault from which geologic slip rates can be developed. Large strike-slip offsets of many tens to hundreds of metres have already been recognised in the Mint to Arthur creek area, and potential single-event displacements have also been recognised southwest of Gaunt Creek (De Pascale and Langridge, 2012b). For large displacements, the proportion of error related to the cell size of the DEM (~±3 m) is small compared to the scale of the displacements. In contrast, the error on single-event displacement values of sub-decametre size recognised from the LiDAR indicates that they will have large uncertainties that make such measurements less meaningful for the fault under dense forest. An outcome of this observation is that while LiDAR has proven itself as a useful remote reconnaissance tool for identifying potential single-event displacements in areas of dense vegetation, there is still no substitute for reconnaissance and measurement of fault parameters in the field.

Along the western part of the Hope Fault, the 2-m LiDAR-derived DEM has improved both the location and mapping of the fault in detail (c.f. Langridge and Berryman, 2005; Nathan et al., 2002). It has also been possible to recognise numerous secondary faults including normal, reverse and oblique-slip faults, that were previously unknown across a wider zone of tectonic deformation that is 100–300 m wide (Khajavi et al., 2012). Importantly, as with the Franz-Whataroa survey, the 2-m LiDAR DEM has given an unprecedented view of offset geomorphic features (e.g. alluvial fans and terraces, channels, spurs) that allow for the robust and routine measurement of dextral-slip offsets along the fault. The improved clarity and error related to the 2-m DEM means that the uncertainties on large offsets (tens to hundreds of metres) are relatively small, while the ability to locate and assess single-event displacements of 3–6 m size with such uncertainties (~±2 m) will be difficult without field verification (Langridge and Berryman, 2005; Langridge et al., 2013).

6. Conclusions

Sub 5-m digital elevation models (DEMs) were derived from airborne LiDAR surveys for active faults in New Zealand under varying degrees of forest cover and relief. In each case, the high-quality bare earth DEMs derived from the LiDAR data allowed us to recognise and map in detail many fault-displaced landforms and other geomorphic features that were previously unknown or poorly resolved. The LiDAR data revolutionises our understanding of fault location and fault structure in these variably forested areas of active deformation.

Project design, flight planning and data processing methodologies that we developed for these areas of especially dense vegetation cover were at times intuitive but provided us with valuable insights and experience. For example, along the rangefront of the central part of the Alpine Fault, reducing the flight line spacing from 275 to 200 m and increasing the amount of data overlap (i.e. two- or three-fold overlap of data coverage) compensates for the low ground returns from the dense native forest cover and steep and gullied terrain allowing us to produce a 3-m DEM. In contrast, a 275 m flight line spacing was adequate to produce a 2-m DEM and sufficient to resolve fault traces and offset geomorphic features along the beech-covered, western part of the Hope Fault.

We used an IDW technique to interpolate the ground return point cloud data. However, based upon the results from previous research, it is apparent that no interpolation method is universally superior. Ground return spacing (which is a function of lidar survey parameterisation and vegetation density), raster spatial resolution, the complexity of terrain morphology, and the assumptions underpinning a given interpolator's mathematical design affect the ability of interpolation algorithms to generate accurate and useful DEMs.

The results of this study will assist in the future planning of airborne LiDAR collection in New Zealand and show the great potential and limitations of LiDAR as a cost-effective, utile tool for the precise mapping and study of active faults and other geomorphic features that are covered by dense old growth forest worldwide. Such results are important for future studies that consider fault segmentation and rupture patterns as part of seismic hazard analyses.

Acknowledgements

The authors wish to thank the Natural Hazards Research Platform for funding this study (NHRP Contract CO5X0702). We also wish to acknowledge the Department of Conservation and local landowners for land access essential to field checking of LiDAR data. Murray Hicks at NIWA is thanked for supplying the rainfall contour data. Phaedra Upton, Jamie Howarth and Salman Ashraf provided reviews on an early version of this paper, and Ben Brooks and Brad Case are warmly thanked for their encouraging input and reviews of the paper.

References

Adams, T., Brack, C., Farrier, T., Pont, D., Brownlie, R., 2011. So you want to use LiDAR? – a guide on how to use LiDAR in forestry. New Zeal. J. For. 55, 19–23.

Arrowsmith, J.R., Zielke, O., 2009. Tectonic geomorphology of the San Andreas Fault zone, from high resolution topography: an example from the Cholame segment. Geomorphology 113, 70–81. http://dx.doi.org/10.1016/j.geomorph.2009.01.002.
Barrell, D.J.A., Andersen, B.G., Denton, G.H., 2011. Glacial Geomorphology of the Central South Island, New Zealand. +map (5 sheets) + legend (1 sheet). In: GNS Science Monograph, 27. GNS Science, Lower Hutt, New Zealand, p. 81.
Barth, N.C., Toy, V.G., Langridge, R.M., Norris, R.J., 2012. Scale dependence of oblique plate boundary partitioning: new insights from LiDAR, central Alpine Fault, New Zealand. Lithosphere 4, 435–448. http://dx.doi.org/10.1130/L201.1.
Beauprêtre, S., Garambois, S., Manighetti, I., Malavieille, J., Senechal, G., Davies, T., Chatton, M., Larroque, C., Rousset, D., Cotte, N., Romano, C., 2012. Finding the buried record of past earthquakes with GPR-based paleoseismology a case study on the Hope fault, New Zealand. Geophys. J. Int. 189, 73–100.
Beavan, J., Denys, P., Denham, M., Hager, B., Herring, T., Molnar, P., 2010. Distribution of present-day deformation across the Southern Alps, New Zealand, from 10 years of GPS data. Geophys. Res. Lett. 37, L16305. http://dx.doi.org/10.1029/2010GL044165.
Begg, J.G., Mouslopoulou, V., 2009. Analysis of late Holocene faulting within an active rift using lidar, Taupo Rift. New Zeal. J. Volcanol. Geotherm. Res. 190, 152–167. http://dx.doi.org/10.1016/j.jvolgeores.2009.06.001.
Berryman, K., Beanland, S., 1988. Ongoing deformation in New Zealand: rates of tectonic movement from geological evidence. Trans. Institut. Prof. Eng. New Zeal. 15, 25–35.
Berryman, K., Alloway, B., Almond, P., Barrell, D., Duncan, R., McSaveney, M., Read, S., Tonkin, P., 2001. Alpine fault rupture and landscape evolution in Westland, New Zealand. In: Proceedings 5th International Conference of Geomorphology, Tokyo, 2001.
Berryman, K.R., Beanland, S., Cooper, A.F., Cutten, H.N., Norris, R.J., Wood, P.R., 1992. The Alpine Fault, New Zealand: variation in Quaternary structural style and geomorphic expression. Ann. Tecton. VI, 126–163.
Bevis, M., Hudnut, K., Sanchez, R., Toth, C., Grejner-Brzezinska, D., Kendrick, E., Caccamise, D., Raleigh, D., Zhou, H., Shan, S., 2005. The B4 Project: Scanning the San Andreas and San Jacinto Fault Zones. Fall Meeting Supplement EOS Trans. Am. Geophys. Union 86 (52).
Chan, Y.-C., Chen, Y.-G., Shih, T.-Y., Huang, C., 2007. Characterising the Hsincheng active fault in northern Taiwan using airborne LiDAR data: detailed geomorphic features and their structural implications. J. Asian Earth Sci. 31, 303–316.
Cox, S.C., Barrell, D.J.A., 2007, 1 sheet+. Geology of the Aoraki Area: Institute of Geological and Nuclear Sciences 1: 250 000 Geological Map, 12. Institute of Geological and Nuclear Sciences, Lower Hutt, New Zealand, p. 65.
Cox, S.C., Sutherland, R., 2007. Regional geologic framework of South Island, New Zealand, and its significance for understanding the active plate boundary. In: Okaya, D., Stern, T., Davey, F. (Eds.), A Continental Plate Boundary: Tectonics at South Island, New Zealand, Geophysical Monograph, 175, pp. 19–46.
Cox, S.C., Stirling, M.W., Herman, F., Gerstenberger, M., Ristau, J., 2012. Potentially active faults in the rapidly eroding landscape adjacent to the Alpine Fault, central Southern Alps, New Zealand. Tectonics 31, TC2011,. http://dx.doi.org/10.1029/2011TC003038.
Cowan, H.A., 1990. Late Quaternary displacements on the Hope fault at Glynn Wye, North Canterbury. New Zeal. J. Geol. Geophys. 33, 285–293.
Cunningham, D., Grebby, S., Tansey, K., Gosar, A., Kastelic, V., 2006. Application of airborne LiDAR to mapping seismogenic faults in forested mountainous terrain, southeastern Alps, Slovenia. Geophys. Res. Lett., L20308.
Dawson, J., Lucas, R., 2011. New Zealand Native Trees. Craig Potton Publishing, Nelson, New Zealand.
De Pascale, G.P., Langridge, R.M., 2012a. New on-fault evidence for a great earthquake in 1717, central Alpine fault, New Zealand. Geology 40, 791–794. http://dx.doi.org/10.1130/G33363.1.
De Pascale, G.P., Langridge, R.M., 2012b. Alpine fault. In: AGU San Francisco 2012.
DeMets, C., Gordon, G., Argus, D.F., Stein, S., 1994. Effect of recent revisions to the geomagnetic reversal time scale on estimates of current plate motions. Geophys. Res. Lett. 21, 2191–2194.
Duffy, B., Quigley, M., Barrell, D.J.A., Van Dissen, R., Stahl, T., Leprince, S., McInnes, C., Bilderback, E., 2013. Fault kinematics and surface deformation across a releasing bend during the 2010 M_W 7.1 Darfield, New Zealand, earthquake revealed by differential LiDAR and cadastral surveying. Geol. Soc. Am. Bull. 125, 420–431. http://dx.doi.org/10.1130/B30753.1.
Frankel, K.L., Dolan, J.F., Owen, L.A., Finkel, R.C., Hoeft, J.S., 2007. Spatial variations in slip rate along the Death Valley-Fish Lake Valley fault system from LiDAR topographic data and cosmogenic ^{10}Be geochronology. Geophys. Res. Lett. 34. http://dx.doi.org/10.1029/2007GL030549.
Harris, R.A., Archuleta, R.J., Day, S.M., 1991. Fault steps and the dynamic rupture process: 2-D numerical simulations of a spontaneously propagating shear fracture. Geophys. Res. Lett. 18 (5), 893–896.
Haugerud, R., Harding, D.J., Johnson, S.Y., Harless, J.L., Weaver, C.S., Sherrod, B.L., 2003. High-resolution lidar topography of the Puget Lowland, Washington – a bonanza for earth science. GSA Today 13 (6), 4–9.
Hodgson, M.E., Jensen, J.R., Schmidt, L., Schill, S., Davis, B., 2003. An evaluation of LIDAR- and IFSAR-derived digital elevation models in leaf-on conditions with USGS Level 1 and Level 2 DEMs. Remote Sens. Environ. 84, 295–308.
Holt, W.E., Haines, A.J., 1995. The kinematics of northern South Island, New Zealand, determined from geologic strain rates. J. Geophys. Res. 100 (17), 991–18010.
Hu, Y., 2003. Automated Extraction of Digital Terrain Models, Roads and Buildings Using Airborne LiDAR Data (PhD thesis). Department of Geomatics Engineering, The University of Calgary, Calgary, Alberta, Canada.
Hudnut, K.W., Borsa, A., Glennie, C., Minster, J.B., 2002. High-resolution topography along surface rupture of the 16 October 1999 Hector Mine, California, earthquake (M-w 7. 1) from airborne laser swath mapping. Bulletin of the Seismological Society of America 92 (4), 1570–1576.
Koehler, R.D., Baldwin, J.N., Prentice, C.S., Pearce, J., 2005. Holocene Geologic Characterization of the Northern San Andreas Fault, Gualala, California. National Earthquake Hazards Reduction Program Final Technical Report, NEHRP External Grant Award Number 03HQGR0045 http://www.earthquake.usgs.gov/research/external/research.php.
Khajavi, N., Langridge, R.M., Quigley, M., 2012. Hope fault. In: AGU, San Francisco 2012.
Koons, P.O., 1990. Two-sided orogen: collision and erosion from the sandbox to Southern Alps, New Zealand. Geology 18, 679–682.
Korup, O., 2006. Effects of deep-seated bedrock landslides on hillslope morphology, Southern Alps, New Zealand. J. Geophys. Res. 111, F01018. http://dx.doi.org/10.1029/2004JF000242.
Langridge, R.M., 2011. Precise Mapping of Near-field Fault Deformation in New Zealand using LiDAR technology. In: Final Report: Hazards Platform Contestable Fund. GNS Science, p. 65. Report 2011/44.
Langridge, R.M., Berryman, K.R., 2005. Morphology and slip rate of the Hurunui section of the Hope Fault, South Island, New Zealand. New Zeal. J. Geol. Geophys. 48, 43–58.
Langridge, R., Ries, W., 2010. Active Fault Mapping and Rupture Avoidance Zonation for the Alpine Fault in West Coast Region. GNS Science Consultancy. Report 2009/18.
Langridge, R., Campbell, J., Hill, N., Pere, V., Pope, J., Pettinga, J., Estrada, B., Berryman, K., 2003. Paleoseismology and slip rate of the Conway segment of the Hope fault at Greenburn Stream, South Island, New Zealand. Ann. Geophys. 46, 1119–1139.
Langridge, R., Duncan, R., Almond, P., Robinson, R., 2007. Indicators of Paleoseismic Activity along the Western Hope Fault. GNS Science Consultancy. Report 2006/151.
Langridge, R., Almond, P., Duncan, R., 2013. Timing of late Holocene paleoearthquakes on the Hurunui segment of the Hope fault: implications for plate boundary strain release through South Island, New Zealand. Geol. Soc. Am. Bull. 125, 756–775. http://dx.doi.org/10.1130/B30674.1.
Langridge, R.M., Berryman, K.R., Van Dissen, R.J., 2005. Defining the geometric segmentation and Holocene slip rate of the Wellington Fault, New Zealand: the Pahiatua section. New Zeal. J. Geol. Geophys. 48, 591–607.
Langridge, R.M., Villamor, P., Basili, R., 2006. Earthquake Fault Trace Survey – Central Hawke's Bay District. Report 2006/98. GNS Science Client, p. 31 (+ appendix).
McMorran, T.J., 1991. The Hope Fault at Hossack Station East of Hanmer Basin, North Canterbury. Unpublished M.Sc. thesis, lodged in the. University of Canterbury Library, Christchurch, p. 239.
Meigs, A., 2013. Active tectonics and LiDAR revolution. Lithosphere 5, 226–229. http://dx.doi.org/10.1130/RF.L004.1.
Nathan, S., Rattenbury, M.R., Suggate, R.P., 2002, 1 sheet +. Geology of the Greymouth Area: Institute of Geological and Nuclear Sciences 1: 250 000 Geological Map, vol. 12. Institute of Geological and Nuclear Sciences, Lower Hutt, New Zealand, p. 65.
Newsome, P.F.J., 1987. The Vegetative Cover of New Zealand. In: Water and Soil Miscellaneous Publication, vol. 112. National Water and Soil Conservation Authority, p. 153. + 2 map sheets.
Norris, R.J., Cooper, A.F., 1995. Origin of small-scale segmentation and transpressional thrusting along the Alpine Fault, New Zealand. Geol. Soc. Am. Bull. 107, 231–240.
Norris, R.J., Cooper, A.F., 1997. Erosional control on the structural evolution of a transpressional thrust complex on the Alpine Fault, New Zealand. J. Struct. Geol. 19, 1323–1342.
Norris, R.J., Cooper, A.F., 2001. Late Quaternary slip rates and slip partitioning on the Alpine Fault, New Zealand. J. Struct. Geol. 23, 507–520.
Norris, R.J., Cooper, A.F., 2007. The Alpine fault, New Zealand: Surface geology and field relationships. In: Okaya, D., Stern, T., Davey, F. (Eds.), A Continental Plate Boundary: Tectonics at South Island, New Zealand. American Geophysical Union, Washington, DC, pp. 157–175.
Oskin, M.E., Arrowsmith, J.R., Hinojosa Corona, A., Elliott, A.J., Fletcher, J.M., Fielding, E.J., Gold, P.O., Gonzalez Garcia, J.J., Hudnut, K.W., Liu-Zeng, J., Teran, O.J., 2012. Near-field deformation from the El Mayor-Cucapah earthquake revealed by differential LIDAR. Science 335, 702–705. http://dx.doi.org/10.1126/science.1213778.
Prentice, C.S., Crosby, C.J., Whitehill, C.S., Arrowsmith, J.R., Furlong, K.P., 2009. Illuminating Northern California's active faults. Eos 90 (7), 55–56.
Quigley, M., Van Dissen, R.J., Litchfield, N., Villamor, P., Duffy, B., Barrell, D., Furlong, K., Stahl, T., Bilderback, E., Noble, D., 2012. Surface rupture during the 2010 M_W 7.1 Darfield (Canterbury) earthquake: Implications for fault rupture dynamics and seismic-hazard analysis. Geology 40, 55–58. http://dx.doi.org/10.1130/G32528.1.
Read, S., 1994. Alpine Fault Segmentation and Rangefront Structure between Gaunt Creek and Little Man River, Near Whataroa, Central Westland, New Zealand. BSc. thesis. Department of Geology, University of Otago, p. 167.
Sieh, K.E., 1978. Slip along the San Andreas fault associated with the great 1857 earthquake. Bull. Seism. Soc. Am. 68, 1421–1448.
Sutherland, R., Berryman, K.R., Norris, R.J., 2006. Quaternary slip rate and geomorphology of the Alpine fault: implications for the kinematics and seismic hazard in southwest New Zealand. Geol. Soc. Am. Bull. 118, 464–474.

Please cite this article in press as: Langridge, R.M., et al., Developing sub 5-m LiDAR DEMs for forested sections of the Alpine and Hope faults, South Island, New Zealand: Implications for structural interpretations, Journal of Structural Geology (2013), http://dx.doi.org/10.1016/j.jsg.2013.11.007

Sutherland, R., Eberhart-Phillips, D., Harris, R.A., Stern, T., Beavan, J., Ellis, S., Henrys, S., Cox, S., Norris, R.J., Berryman, K.R., Townend, J., Bannister, S., Pettinga, J., Leitner, B., Wallace, L., Little, T.A., Cooper, A.F., Yetton, M., Stirling, M., 2007. Do great earthquakes occur on the Alpine Fault in central South Island, New Zealand? In: Okaya, D., et al. (Eds.), A Continental Plate Boundary: Tectonics at South Island, New Zealand, Geophysical Monograph, vol. 175. American Geophysical Union.

Sutherland, R., Toy, V.G., Townend, J., Cox, S.C., Eccles, J.D., Faulkner, D.R., Prior, D.J., Norris, R.J., Mariani, E., Boulton, C., Carpenter, B.M., Menzies, C.D., Little, T.A., Hasting, M., De Pascale, G.P., Langridge, R.M., Scott, H.R., Reid Lindroos, Z., Fleming, B., Kopf, A.J., 2012. Drilling reveals fluid control on architecture and rupture of the Alpine Fault, New Zealand. Geology 40, 1143–1146. http://dx.doi.org/10.1130/G33614.1.

Van Dissen, R., Yeats, R., 1991. Hope fault, Jordan thrust, and uplift of the Seaward Kaikoura Range, New Zealand. Geology 19, 393–396.

Wallace, L.M., Beavan, R.J., McCaffrey, R., Berryman, K.R., Denys, P., 2007. Balancing the plate motion budget in the South Island, New Zealand using GPS, geological and seismological data. Geophys. J. Int. 168, 332–352. http://dx.doi.org/10.1111/j.1365-246X.2006.03183.x.

Wallace, R.E., 1968. Notes on stream channels offset by the San Andreas fault. In: Dickinson, W.R., Grantz, A. (Eds.), Proceedings of Conference on Geologic Problems of the San Andreas Fault, Stanford University Publications in the Geological Sciences, vol. 11, pp. 6–21.

Wardle, J., 1984. The New Zealand beeches: Ecology, Utilisation and Management. New Zealand Forest Service, Wellington, pp. 31–45.

Wells, A., Duncan, R.P., Stewart, G.H., 2001. Forest dynamics in Westland, New Zealand: the importance of large, infrequent earthquake-induced disturbance. J. Ecol. 89, 1006–1018.

Wells, A., Yetton, M.D., Duncan, R.P., Stewart, G.H., 1999. Prehistoric dates of the most recent Alpine fault earthquakes, New Zealand. Geology 27, 995–998.

Wesnousky, S.G., 2006. Predicting the endpoints of earthquake ruptures. Nature 444 (7117), 358–360.

Yeats, R., Berryman, K.R., 1987. South Island, New Zealand, and Transverse Ranges, California: A seismotectonic comparison. Tectonics 6, 363–376.

Yetton, M.D., 2000. The Probability and Consequences of the Next Alpine Fault Earthquake, South Island, New Zealand. Doctor of Philosophy thesis. Dept. of Geological Sciences, University of Canterbury, Christchurch, New Zealand.

Zachariasen, J., Prentice, C.S., 2008. Detailed Mapping of the Northern San Andreas Fault Using LiDAR Imagery. Award Number 05HQGR0069. U.S. Geological Survey National Earthquake Hazards Reduction Program, p. 47.

Zielke, O., Arrowsmith, J.R., Grant Ludwig, L., Acsiz, S.O., 2010. Slip in the 1857 and earlier large earthquakes along the Carrizo Plain, San Andreas Fault. Science 327, 1119–1122.